

Metamaterials of Fluids of Light and Sound

D. L. Chafatinos,^{1,2} A. S. Kuznetsov,³ P. Sesin,^{1,2} I. Papuccio,^{1,2} A. A. Reynoso,^{1,2}
A. E. Bruchhausen,^{1,2} G. Usaj,^{1,2} K. Biermann,³ P. V. Santos,³ and A. Fainstein^{1,2,*}

¹Centro Atómico Bariloche and Instituto Balseiro,

Comisión Nacional de Energía Atómica (CNEA) - Universidad Nacional de Cuyo (UNCuyo), 8400 Bariloche, Argentina.

²Instituto de Nanociencia y Nanotecnología (INN-Bariloche),

Consejo Nacional de Investigaciones Científicas y Técnicas (CONICET), Argentina.

³Paul-Drude-Institut für Festkörperelektronik, Leibniz-Institut im Forschungsverbund Berlin e.V., Hausvogteiplatz 5-7, 10117 Berlin, Germany.

(Dated: November 29, 2021)

Phonons, the quanta of vibrations, determine equilibrium and dynamical properties of matter, their material phase and thermal and electronic transport. GHz coherent phonons can interact with and act as interconnects of a wide range of quantum systems. Harnessing and tailoring their coupling to opto-electronic excitations thus becomes a challenge for engineered materials relevant for quantum technologies. With this perspective we introduce polaromechanical metamaterials, two-dimensional arrays of μm -size zero-dimensional traps confining light-matter polariton fluids and GHz phonons. These metamaterials integrate strongly interacting phonon-polariton oscillators at the lattice sites with inter-site coupling mediated by optomechanical interactions, with remarkable consequences for the lattice dynamics. When locally perturbed by optical excitation, they respond locking the energy detuning between neighbor sites at integer multiples of the phonon quantum, evidencing synchronization blockade and a collective behaviour of the polariton and phonon fields. These results open the path for the coherent control of quantum light fluids with hypersound in a scalable platform.

I. INTRODUCTION

Microcavity exciton-polariton fluids of light (the quantum states formed by strongly coupled excitons and photons in microcavities) constitute a hybrid system¹ that displays a plethora of striking properties. These include Bose-Einstein condensation (BEC),² superfluidity,³ and Josephson-like oscillations,^{4,5} with peculiarities stemming from the involved exciton mediated repulsive Coulomb interactions and the driven-dissipative non-Hermitian nature of the fluid.⁶ The light-matter strong-coupling coherently connects the optical domain (100's of THz) with inter-band optoelectronic excitations.¹ The engineering of coupled pairs of polariton traps^{4,5} and arrays^{2,7,9} with controllable interactions¹⁰ has attained a degree of maturity that enables the implementation of quantum simulators^{11–14} and topological photonics¹⁵. Optomechanical crystals (OMXs)^{16–19} are another kind of hybrid structures that bridge the optical domain with acoustics (MHz-GHz-range). OMXs exploit the Bragg co-localisation of mechanical and optical modes to greatly enhance their interaction. Interestingly, cavity optomechanics has also been exploited to induce gauge fields as a resource for effectively breaking the time-reversal symmetry in topological photonics^{20–22} and phononics.^{23,24} In this field one active trend is the search for the ultra-strong coupling regime, characterized by an optomechanical coupling rate exceeding the decay rates of phonons and light, as well as the phonon frequency.^{25–27} The question then naturally arises: can the powerful developments of optomechanics be used to actuate on polariton systems relevant for optoelectronics and quantum technologies? Moreover: can the behaviour of driven-dissipative light

fluids be intertwined with coherent vibrations in a lattice to yield a collective behaviour qualitatively different from that of its individual components? We address these questions and answer them positively in this work.

Polariton condensates are of great relevance in cavity optomechanical phenomena due to their long coherence times and the resonantly-enhanced exciton-mediated optomechanical coupling.^{6,21,29,30} Both parameters are critical to boost the optomechanical cooperativity.¹⁸ It has been shown that the same GaAs/AlAs-based planar microcavities leading to cavity polaritons, also confine hypersound in the 20 GHz range.⁶ Inspired then by the idea of OMXs^{16–19}, we go beyond the concept of Bragg structures and propose metamaterials based on resonant unit cells.³² These consist of micrometer-size 0D intra-cavity polariton traps^{2,3} that confine and co-localize polaritons and acoustic vibrations, as well as in arrangement of such “polaromechanical” individual resonators into crystal arrays (see the AFM image of an actual array and the scheme in Figs. 1a and b, respectively). The concept of polaromechanical metamaterials becomes particularly powerful in the regime of negligible Josephson-like inter-site coupling (relatively large inter-trap separations). In this regime, the on-site optomechanical interactions lead to a phonon-mediated strong inter-trap tunnelling mechanism of the polariton condensates. Striking signatures of the coherent polariton-phonon coupling emerge in this case when the structures are optically driven with a continuous non-resonant and spatially localized optical excitation close to and above the threshold for condensation. Namely, the ground-states of polariton condensates at neighbor traps asynchronously lock with energies differing by integer numbers of the phonon quanta, as illus-

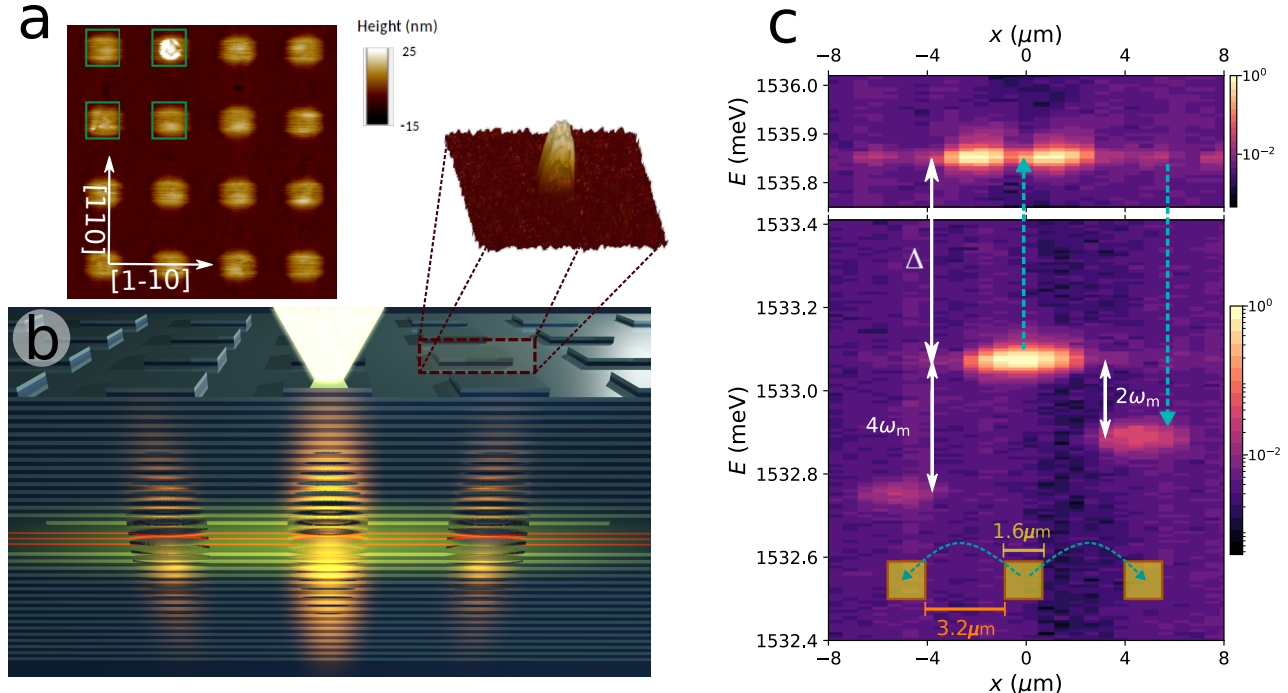


Figure 1. **Polaromechanical metamaterials.** Panel **a** is a 2D (top-view) atomic-force microscope (AFM) image of an array of $1\mu\text{m}$ square intra-cavity traps separated by $1\mu\text{m}$ -wide barriers. The observed rounding of the structures results from the overgrowth of the top-DBR. A scheme of the microcavity patterned with square-shape micrometer-size traps is presented in panel **b**. The three red lines in the spacer represent the quantum wells where excitons are hosted. The spacer thickness is larger at the position of the traps. The laser focuses on one of the traps, leading to coupled polaritons and vibrations in the individual unit cells of the array. The inset shows an AFM image of an individual $2 \times 2\mu\text{m}^2$ square trap. Panel **c** shows the spatially resolved emission spectra obtained for such focused non-resonant excitation with powers above the polariton condensation threshold, for a square array of $1.6\mu\text{m}$ square traps separated by $3.2\mu\text{m}$ barriers. The central trap ($x = 0$) and the two closest neighbors ($x \pm 4.8\mu\text{m}$) can be identified. Both s-like symmetry ground ($\sim 1533\text{ meV}$) and p-like symmetry excited ($\sim 1535.9\text{ meV}$) states of polaritons in the traps are observed. Note that the neighbor trap ground state energies asynchronously lock at relative detunings corresponding to $\delta E \sim -2\hbar\omega_m$ and $\delta E = -4\hbar\omega_m$, where ω_m is the confined phonon frequency. The dashed blue-arrows represent the optomechanically-induced inter-trap coupling mediated by the excited-state.

trated in Fig. 1c. In order to explain this notable result we begin by describing the polariton and phonon bands of polaromechanical arrays. We then zoom into the behavior of single traps and coupled double traps to disclose how such bands emerge from the resonant unit cells. Finally, the characteristics of the novel asynchronous locking phenomenon are analysed, followed by a discussion and outlook.

II. RESULTS

Polaromechanical metamaterials: co-localised polariton and phonon bands in lattices of 0D resonators. The proposed new system is based on μm -sized traps previously studied in the context of polariton phenomena,^{2,3} and created by micro-structuring the spacer of an (Al,Ga)As microcavity in between growth steps by molecular beam epitaxy (MBE). Regions of narrow (etched regions, ER) and wider (non-etched region, nER) microcavity spacer thickness give rise to optical cavity modes of higher or lower energy, respectively (see

details in the Supplementary Material I). These provides the means to define traps and barriers in spatially tailored effective potentials. The etching is performed in a layer away from the quantum wells (QWs) so that the quality of the resulting excitonic system remains conserved. The magnitude of the effective potential modulation acting on the polaritons (typically some meV) is determined by the spacer etching thickness (typically around 10-15 nm), and by the cavity-exciton detuning.

Panels a and b in Fig. 2 present the 2D polariton in-plane energy dispersion (i.e., along the $k_x - k_y$ plane) for 10×10 arrays of $4 \times 4\mu\text{m}^2$ and $1 \times 1\mu\text{m}^2$ square traps, respectively, in both cases separated by $1\mu\text{m}$ barriers. These dispersions were measured by angular-resolved photoluminescence (PL) at low temperatures (5 K), under non-resonant excitation ($\lambda \sim 760\text{ nm}$) with low optical powers (i.e., well below the BEC threshold). The full array was homogeneously illuminated with a large spot of $\sim 50\mu\text{m}$ diameter. The larger 4×4 traps confine several states with energies below the finite barriers³. When organized in arrays this results in the formation of several bands, as displayed in Fig. 2a. The lower energy

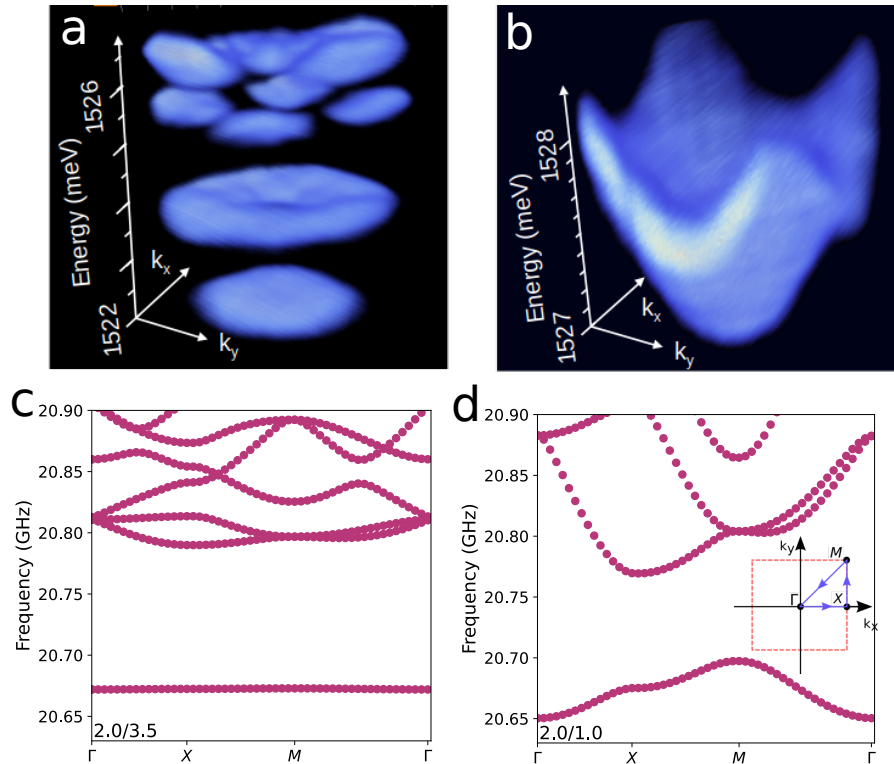


Figure 2. Polariton and phonon bands in lattices of 0D resonators. Panels **a** and **b** present the spectrally and wavevector resolved polariton energies obtained by photoluminescence at low excitation powers in lattices of $4 \times 4 \mu\text{m}^2$ and $1 \times 1 \mu\text{m}^2$ square traps, respectively, both with $1 \mu\text{m}$ -wide barriers. The larger 4×4 traps display several confined modes, while only the ground state is confined for the smaller 1×1 structures. Panels **c** and **d** display the calculated in-plane dispersion of the acoustic modes of lattices of $2 \times 2 \mu\text{m}^2$ square traps separated by $1 \mu\text{m}$ and $3.5 \mu\text{m}$ -wide barriers, respectively.

band derives from trap states of s-like symmetry, and is comparatively flat due to the larger degree of confinement (lower hybridization with neighbor traps) of these states. In contrast, the smaller 1×1 traps only confine the ground state, the other levels forming part of the continuum above the barrier edge. The reciprocal space dispersion in this case (Fig. 2b) resembles the one for dispersive electron bands in a tight-binding model, where the role of the atomic electron level is played by the discrete polariton ground state of the 0D traps.

As mentioned above, vibrations are also confined in planar microcavities⁶, with fundamental frequency $\nu_m \sim 20$ GHz corresponding to a breathing of the cavity layer along the growth direction. The wavelength of these confined phonons is the same as the one for the confined photons (determined by the cavity spacer thickness). The frequency difference (from tens of GHz for the phonons to hundreds of THz for the photons) just bears the relation between the respective wave speeds. A local etching of the spacer thickness blue-shifts the phonon mode energy in the same proportion as for the confined photons (see Supplemental Material IVA) and, consequently, it is to be expected that an effective lateral potential will develop for the confined acoustic phonons as it does for the polaritons. The calculated *phonon* dispersion around the Γ point of the Brillouin zone ($k_x = k_y = 0$) for arrays of

$2 \times 2 \mu\text{m}^2$ traps with $\sim 3.5 \mu\text{m}$ and $\sim 1 \mu\text{m}$ -wide barriers are presented in Figs. 1c and d, respectively (the model used is described in the Methods section). Phonon bands arise for the 2D lattice of traps and, mimicking what was observed for the polaritons, the lower energy band is flatter for the case of more isolated ground states. Note that for the polariton dispersions presented in Figs. 2a and b the width of the bands is tuned by the size of the traps, while for the calculated phonon bands in Figs. 1c and d this same objective is accomplished by changing the barrier width.

Experimental study of phonon confinement in traps, molecules and arrays of coupled traps. Figure 3 resumes a detailed experimental study of the phonons confined in individual square traps, molecule-like double-traps, and in arrays of traps. The spatial distribution of the mechanical fundamental eigenmode (~ 20 GHz) calculated using finite elements is shown in panel a (see the Supplementary Material IVB). This was done for the simplest geometry consisting of a circular trap at the center of a cylindrical pillar limited by vacuum. It is conceptually similar to the square trap, but computationally simpler because the rotation symmetry requires solving only a 2D problem. Full consideration of the sample layer structure is included as prescribed by the MBE process. The trap is modelled as a central $5 \mu\text{m}$

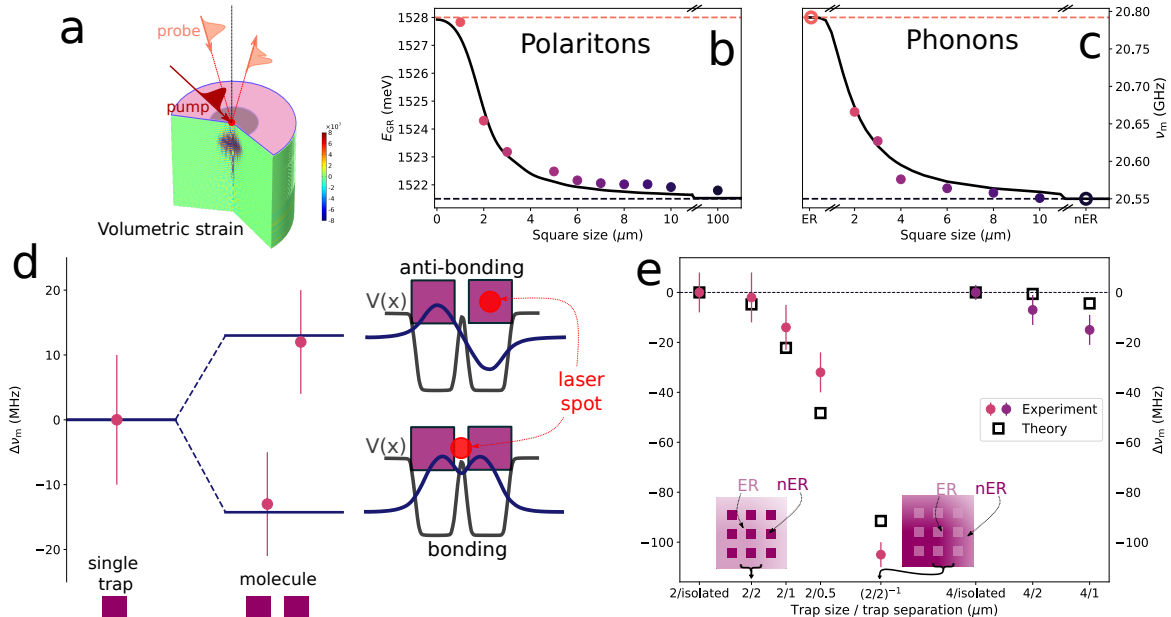


Figure 3. Experimental study of confined phonons in traps and lattices of traps. Panel a shows the finite-element 3D modelling of the spatial distribution of the volumetric strain associated to the fundamental confined acoustic mode of an individual circular trap of $5\mu\text{m}$ diameter. The cylinder is the full modelled region, much larger than the trap (the non-etched region is indicated with the darker color in the top). A scheme of the experimental pump and probe method used to study the confined phonons is included (see text for details). Panel b(c) presents the measured size dependence of the polariton(phonon) ground confined mode in a square trap. The limits of the induced potential, corresponding to planar etched (barrier) and non-etched (well) regions are indicated by the dashed horizontal lines. The continuous black curve is the effective potential model. The case for a molecular-like phonon double-trap made of two $2 \times 2\mu\text{m}^2$ traps separated by $0.5\mu\text{m}$, is illustrated in panel d. The phonon potential, and the calculated bonding and anti-bonding-like levels are shown, together with a scheme of the respective excitation condition at different sites. Symbols correspond to the experiments, while the solid lines are the theoretical predictions. Panel e summarises the phonon experiments on arrays of traps of 4 and $2\mu\text{m}$ lateral size, with different inter-trap separation, and their comparison with the effective potential model. Again the energies are given with respect to that of the corresponding single trap (identified as “2/isolated” and “4/isolated” in this panel). The arrays are labeled as a/b , with a the trap size, and b the inter-trap separation. The case of an inverted array of $2\mu\text{m}$ etched regions separated by $2\mu\text{m}$ non-etched regions (labeled as $(2/2)^{-1}$) is also included. Circular full (square empty) symbols are the experimental (theoretical) values.

diameter nER with larger spacer thickness (indicated in the top of the figure with a darker color). The color coded acoustic amplitudes clearly show that the traps indeed confine phonons in 0D, in much the same way as they confine light: i.e., the Bragg reflectors strongly confine the phonons along the growth direction, while the microstructuring of the spacer thickness creates an effective lateral potential that confines the phonons in the remaining two dimensions.

Panels b and c in Fig. 3 present a comparative study of the polariton and phonon ground-state energy for *isolated* traps of varying square size. The polariton energies in panel b were obtained from PL data recorded at 5 K under low excitation power (i.e., well below BEC). ³ The trap spectra correspond to discrete levels, the number of confined states depending on the size of the traps (only data for the ground state are presented in Fig. 3b). The limits of the induced potential, corresponding to measurements performed on planar etched (barrier) and non-etched (well) regions are indicated by the dashed horizontal lines. The expected size-dependence for a trap

ping potential with finite barrier height is observed. The experimental data are compared in Fig. 3b with a theoretical calculation based on an effective potential model with a realistic description of the trap potential³ (black solid curve, see Supplemental Material IVC for details), showing excellent agreement.

To experimentally study the high frequency vibrations in the same traps, we used a picosecond coherent phonon pump and probe technique⁴ adapted to semiconductor multilayers⁵ and, specifically, to take profit of the optical resonance in microcavities¹¹. Traps were individually addressed using a microscope set-up with a $\sim 3\mu\text{m}$ -wide Gaussian spot. The concept is illustrated by the scheme in Fig. 3a and in more details in the Methods section. The larger black and red open dots in Fig. 3c are the measurements in extended planar nER and ER regions, respectively. These define, as for the polariton case discussed above, the limits of the induced lateral phonon effective potential (traps and barriers, respectively). Within these limits the phonon trap energies increase with decreasing size, as expected for confined

states in a trap with finite barriers (examples of experimental spectra are provided in the Supplementary Material III). The observed shift is very well described by a phonon effective potential model (black solid curve) based precisely on the same parameters for the traps as used to describe the polariton energies (see the Methods section). The similarity with the behavior of polaritons in Fig. 3b emphasises the concept of polaromechanical traps in which both polaritons and phonons are confined in 0D resonators. We note that confined polaritons and phonons have been detected in traps with dimensions down to $1 \times 1 \mu\text{m}^2$, and that these exhibit record coherence times for polariton condensates (ns-long) and for confined phonons (100's ns) with no observable reduction with decreasing trap size.

We now turn to architectures of coupled 0D resonators. Experiments demonstrating the formation of polariton bands were described in Figs. 2a and b, we concentrate here on the phonon properties. The case of a molecule-like structure made of two $2 \times 2 \mu\text{m}^2$ traps separated by $0.5 \mu\text{m}$ is presented in Fig. 3d. The symbols correspond to the experimental values, and the horizontal lines are the calculated energies (see the Supplemental Material IVC). To selectively excite each state we positioned the laser spot either symmetrically between the traps, or on top of one of them (as shown in the scheme of Fig. 3d). Two states of anti-bonding and bonding character arise, split relative to the individual trap by the interaction energy $\pm J$. The modelled effective phonon potential corresponding to the double-trap structure is also shown, together with the calculated spatial shape of the resulting bonding and anti-bonding states. The measured splitting of the modes, and their ordering (bonding state at lower energy), are in excellent agreement with the theory.

Figure 3e summarizes experiments on a series of arrays of square traps of 2 and $4 \mu\text{m}$ lateral size, and different inter-trap distance. These are labeled as a/b , where $a(b)$ identifies the trap size(separation) in μm . An “inverted” array is also included, corresponding to etched squares of $2 \times 2 \mu\text{m}^2$ size, separated by $2 \mu\text{m}$ -wide nER channels [labeled as $(2/2)^{-1}$]. All frequencies are given with respect to that of the respective isolated single trap. The measured frequencies are also compared to those calculated for the Γ point “s”-like vibrations (i.e., the lower energy mode at $k_y = 0$ in Figs. 2c and d), shown with open squares in Fig. 3e. Due to the experimental geometry with light incident within a small cone around the normal direction, the probe pulse couples with $k \sim 0$ vibrations. Since, in addition, the spatial distribution of the Gaussian pulse is uniform at the scale of an individual trap, it is sensitive to the more symmetric “s”-like ground state. Note that the observed red-shift of the detected modes with decreasing inter-trap separation (e.g, from $2/2$ to $2/0.5$) is a measure of the array phonon half band-width. For inter-trap separations $\gtrsim 2 \mu\text{m}$ the Γ point mode is almost coincident in frequency with that of the individual trap, signalling the flat-band limit. Note also the weaker red-shift of the Γ point mode of the $4 \mu\text{m}$ trap lattices,

when compared to those constructed from $2 \mu\text{m}$ traps, reflecting the relatively flatter-band nature of the former. Indeed, as for the polariton bands in Fig. 2a, for larger traps the on-site energies are smaller and, consequently, red-shifted farther down from the barrier edge. Consequently, the states become less delocalised when traps are coupled in an array. Several additional examples of the dispersion of phonon modes in arrays of different trap sizes and separations can be seen in the Supplementary Material IVC.

Driven polaromechanical crystals: asynchronous energy locking. We study next the polariton dynamics in these polaromechanical metamaterials inducing their in-plane propagation by optical driving one of the traps with power close to and above the threshold for BEC. This is done through non-resonant optical excitation with the $\sim 3 \mu\text{m}$ diameter laser focus. A Gaussian shape exciton reservoir is formed, and the related Coulomb repulsion is expected to determine the local energies (and thus the dynamics) of polaritons in the traps.³⁷ Quite notably, however, as shown in Fig. 1c for an array of $1.6 \mu\text{m}$ traps separated by $3.2 \mu\text{m}$ barriers, the neighbour site polariton condensate energies do not follow a simple Gaussian distribution but lock at detunings that correspond to integer multiples of the mechanical phonon frequency ω_m .

Indeed this striking result is not an exception but the rule, as further shown in Fig. 4 with a similar experiment in a different square array of $1.3 \mu\text{m}$ square traps separated by $2.6 \mu\text{m}$ barriers. Figures 4a-d present energy-resolved spatial images for increasing non-resonant excitation power, obtained from one row of traps aligned along the crystal direction Y [-1 -1 0]. At very small powers, three traps characterized by relatively broad lines are observed approximately at the same ground state energy (the central trap is at $0 \mu\text{m}$, the closest neighbours appear at $\sim \pm 4 \mu\text{m}$). As the power increases two of the traps blue-shift (panels a-c), as expected from the Coulomb repulsion with the exciton reservoir, the third remaining farther away in energy. This asymmetry between left and right traps arises from a slight involuntary misalignment of the laser spot towards one of the neighbours. As the modes shift with increasing pump power, a clear line-narrowing and non-linear increase of intensity signals the transition to the condensation of the light fluid above a threshold power (P_{th}). At the highest powers, the blue-shift saturates due to higher order non-linearities. Note that the energy of the neighbor trap that also blue-shifts gets rapidly locked with increasing power at a detuning that corresponds to three times the phonon frequency (see the high-power spectra displayed in Fig. 3e). Figures 4f-i display the corresponding spatial images from the same array, but now for a row of traps aligned along the orthogonal crystal direction X [-1 1 0] (square traps grow with a slight rectangular asymmetry, so that the coupling along Y is somewhat larger than along X³). The blue-shift and saturation of the modes with increasing excitation power is observed, again par-

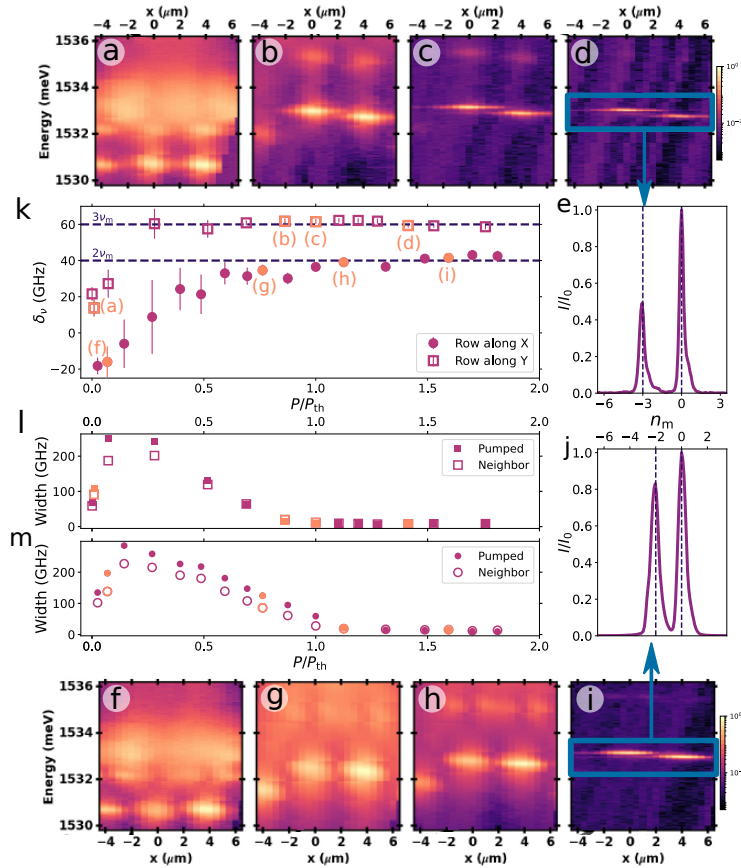


Figure 4. **Polaromechanics: asynchronous locking.** Excitation power dependence of the polariton emission spectra for an array of square traps of $1.3\mu\text{m}$ lateral size separated by $2.6\mu\text{m}$ -etched regions. Examples of energy-resolved spatial images for some selected pump powers are shown in panels **a-d** for a row of traps along the crystal direction Y [-1 -1 0] (see the AFM image in Fig. 1a). The spectrum corresponding to high-powers is displayed in panel **e** (the vertical dashed line indicates an integer number of phonon quanta). A similar sequence of spatial images and high-power spectrum corresponding to a row of traps along the orthogonal direction X [-1 1 0], are shown in panels **f-j**. Panel **k** summarizes the frequency detuning between the pumped and a neighbor trap as a function of pump power (given in terms of P_{Th} , the condensation threshold power), for the two studied cases. The symbols corresponding to the shown spatial images are differentiated with orange color. Panel **l(m)** is the power dependence of the emission linewidth corresponding to the pumped (solid symbol) and most intense neighbor trap (empty symbol) for the data taken along $Y(X)$. In panels **k-m** circles represents measurements along X , and squares along Y .

ticularly for two of the traps that evolve in energy close one to the other. A similar line narrowing and intensity increase accompanies polariton condensation and, again, as evidenced by the high-power spectrum in Fig. 4j the neighbor trap detuning locks at an integer number of the phonon energy quanta (two in this experiment).

The full power dependence of the detuning between the most intense neighbor trap and the central one for the two reported cases (along X displayed with circles, and along Y shown with squares), is shown in Fig. 4k further illustrating the locking at integer numbers of the phonon energy quanta. Figures 4l and 4m present the corresponding linewidth as a function of optical excitation power. Solid(open) symbols correspond to the central(neighbor) trap. For both experiments, at low powers the linewidth of the central trap emission is larger than that of the neighbor trap. This presumably arises due to the Coulomb interaction with the reservoir that is more populated (and thus has larger fluctuations) at the po-

sition of the central trap. Notably, once polaritons in the two traps asynchronously lock their linewidths become identical [around $P/P_{\text{th}} \sim 0.5(1)$ for the experiment along $Y(X)$]. Moreover, polaritons in the two traps condense at the same applied power. For decoupled traps P_{th} should be determined by the local exciton reservoir population, which is different for the two traps. The common linewidth and simultaneous condensation thus provide strong evidence that the polaritons belonging to neighbor traps couple in a single coherent state when they condense and asynchronously lock mediated by the phonon induced coupling.

The presented results evidence a very strong interaction between polaritons and phonons in these resonant polaromechanical metamaterials. We have observed that the confined vibrations play a particularly relevant role in the described collective dynamics when the direct Josephson-like coupling between the ground states of neighbour traps is relatively small, i.e. in the flat-band

limit discussed in the previous sections. It can be shown via second-order perturbation theory that in this case a phonon-induced inter-site *quadratic* optomechanical coupling $g^{(2)}$ arises, due to the on-site linear optomechanical coupling g_0 between the isolated polariton ground states and an extended p-like excited level at energy Δ above the ground state (see the scheme in Fig. 1c).³⁸ For small traps, as those leading to the locking behavior shown in Fig. 1c and Fig. 4, the involved p-like state at $\Delta \sim 3$ meV is indeed shared by both sites. For this case it follows that $g^{(2)} = g_0^2/\Delta$.³⁸ The concept of a polaromechanical metamaterial thus becomes central in this regime, because the polariton inter-trap coupling is determined by the on-site optomechanical interactions of the hybrid metamaterial resonant unit-cell.

The exciton-mediated deformation-potential optomechanical on-site coupling is estimated from Ref. 21 to be $g_0/2\pi \sim 50$ MHz, i.e., three orders of magnitude larger than that due to radiation pressure interaction (see the Methods section). For a driven cavity the single polariton g_0 is amplified as $g_{\text{eff}} = g_0 \sqrt{N_p}$,¹⁸ with N_p the polariton occupation ($N_p \sim 10^6$ in the condensed phase⁷). Consequently, $g_{\text{eff}}/2\pi \sim 50$ GHz. This value brings the system into the so-called ultra-strong-coupling regime,^{25–27} where the polariton-phonon coupling rate becomes much larger than the phonon and polariton decay rates ($\Gamma_m \sim 50$ MHz and $\kappa \sim 1$ GHz), but also larger than the phonon frequency ($\omega_m/2\pi \sim 20$ GHz). Based on these considerations, we estimate for the inter-site quadratic single-polariton coupling $g^{(2)}/2\pi \sim 10^4$ Hz. This value is two orders of magnitude larger than quadratic optomechanical couplings previously reported in specifically designed photonic crystal optomechanical cavities.³⁸ Again, when the traps are driven, a multi-polariton quadratic optomechanical coupling can be defined as $g_{\text{eff}}^{(2)} = g^{(2)} \sqrt{N_p^1 N_p^2}$, where N_p^i is the polariton occupation of trap i (central or neighbor traps).⁷ This implies that for $\sqrt{N_p^1 N_p^2} > 10^5$ the system satisfies $g_{\text{eff}}^{(2)} > \kappa$, a condition experimentally attained when the polaritons evolve with increasing power to the condensed phase.⁷ In this regime the phonon-induced inter-trap tunneling rate becomes faster than the decay rate of the condensates, quantitatively justifying the interpretation of the results as evidence of a collective polaromechanical state.

III. DISCUSSION AND OUTLOOK

Synchronisation between distant polariton condensates has been theoretically proposed,⁴⁰ and also experimentally observed.^{41–43} Indeed synchronisation is a quite general behaviour intimate to dynamical non-linear systems, and pervasive to very different domains of nature.⁴⁴ Interestingly, when the deep quantum limit is attained, energy quantisation hinders synchronisation of identical *non-linear* oscillators.⁴⁵ Interaction requires an exchange

of energy, and in the quantum regime the possible quanta of energy are discrete. If the extractable energy of one oscillator does not exactly match the amount that the second oscillator may absorb, interaction, and thereby synchronisation, is blocked. Polariton condensates are single quantum coherent states, but they are not in the deep quantum regime in the sense that they contain a large number of particles. However, a similar phenomenon emerges because of i) the intrinsic non-linearity of the system required for the asynchronous locking, ii) the inter-trap coupling that is mediated by vibrations, and iii) the BEC linewidth that is much smaller than the phonon frequency. In the polaromechanical metamaterials the polariton condensates and the phonon fields become intimately intertwined in a collective mode that involves the exchange of energy in finite amounts given by the confined phonon energy quanta. The fact that the number of exchanged quanta is $n > 1$ is consistent with a higher-order non-linear phonon-mediated coupling between the polariton condensates of neighbour traps, as proposed here.^{7,18}

In summary, we have demonstrated a new concept for polaromechanical metamaterials, based on planar arrays of traps that confine, co-localise, and strongly couple vibrations and polariton light fluids. The building blocks are micron-size high-Q resonators for polaritons and sound, that can be arranged and inter-linked in arbitrary tailored architectures. The involvement of polariton condensates assures very long coherence times, and leads through an exciton-mediated resonant interaction to hugely enhanced optomechanical couplings. Novel phenomena arise in these polaromechanical crystals, particularly the asynchronous locking of condensed light fluids from neighbour traps at detunings that scale with integer numbers of phonon energy quanta. This evidences a coherent collective dynamics of the polariton and phonon fields, opening the path to novel hybrid scalable platforms applicable for the bi-directional coherent conversion of light-to-microwaves in the 20 GHz frequency range, and for the ultrafast coherent mechanical control of light fluids in quantum technologies.

METHODS:

Photoluminescence spectroscopy. For the polariton PL experiments in the traps at 5–10 K, an external cavity-stabilized *cw* Spectra Physics Ti-Sapphire Matisse laser was used for the non-resonant excitation at ~ 760 nm. The wavevector dependent energy dispersions in Fig. 2 were obtained by exciting the trap-arrays with a large $\sim 50\mu\text{m}$ laser spot, using small optical powers well below the condensation threshold. The wavevector dependence of the spectra was determined with standard methods based on angle-resolved light collection. The optical driving of the condensates to observe the reported asynchronous locking phenomena (Figs. 1c and 4) was performed through focused excitation purposely

centred in one of the central traps of the array using microscope optics to reduce the spot size down to $\sim 3\mu\text{m}$. The same microscope objective (NA=0.4) was used to collect the emitted light. In this latter case a triple additive Jobin-Yvon T64000 spectrometer was used to obtain the required high spectral resolution ($\sim 0.15\text{ cm}^{-1} \sim 20\text{ \mu eV}$).

Pump and probe phonon spectroscopy. A ps-laser pulse is used to resonantly excite the optical cavity mode. A rapid change of index of refraction is induced by the pump through carrier excitation. In addition to this electronic response, the pump pulse launches coherent phonons by a displacive mechanism.^{8,9} These mechanical oscillations modulate the cavity energy through two mechanisms, interface displacement and photoelastic interaction, which are detected using a delayed probe pulse that samples the cavity's reflectivity. A typical spectrum displays characteristic lines corresponding to the $\sim 20\text{ GHz}$ fundamental confined breathing mode of the structures, and weaker contributions at the higher energy overtones at $\sim 60\text{ GHz}$ and $\sim 100\text{ GHz}$ (see the Supplementary Material II). More details are provided in Supplementary Material II.

Effective potential phonon modelling. We assume the non-etched effective quadratic dispersion relation arising when k_z is quantized, i.e., $E(k_x, k_y) = E_{\text{cav,ne}} + \hbar^2(k_x^2 + k_y^2)/(2m_{\text{eff}})$, with homogenous in-plane speed of sound v_s defining an effective mass $m_{\text{eff}} = E_{\text{cav,ne}}/v_s^2$. This is incorporated in a 2D Schroedinger-like equation,

$$(-\hbar^2/(2m_{\text{eff}})\nabla^2 + E_{\text{cav,ne}} + V_e(x, y))\Psi(x, y) = E\Psi(x, y)$$

, that adds the potential $V_e(x, y)$ to effectively describe the trapping induced by the etching. The full height of the potential in an etched zone is $V_{\text{max}} = (E_{\text{cav,e}} - E_{\text{cav,ne}})$, with $E_{\text{cav,e}}$ the energy of the phonon mode in a large etched region. Each square trap i , centered in (x_i, y_i) contributes to $V_e(x, y)$ the potential $V_i(x, y) = V_{\text{max}}(1 - v_i(x - x_i)v_i(y - y_i))$ where the trap profile along each direction is given by $v_i(\alpha) = \frac{1}{2} \left(\text{erfc}\left(\frac{\alpha - \frac{w_i}{2}}{0.55\delta_i}\right) - \text{erfc}\left(\frac{\alpha + \frac{w_i}{2}}{0.55\delta_i}\right) \right)$ with w_i the trap width and δ_i the 10% to 90% transition length. The

eigenvalue problem is solved using finite differences by the customary approach of imposing periodic conditions fulfilling the Bloch theorem. For the width of the nER to ER transition regions, we take $0.35\mu\text{m}$, consistent with both the modelling of the polariton properties and STM studies in similar structures. More details and examples of the calculated phonon dispersion in trap arrays can be found in Supplementary Material IVC.

Estimation of the optomechanical coupling g_0 . Electrically generated mechanical waves have been used in individual similar traps to obtain $g_{\text{om}}/2\pi = \Delta E_{\text{p}}/\Delta u \sim 50\text{ THz/nm}$ ²¹ (change of polariton energy ΔE_{p} per unit displacement Δu). This parameter is related to the on-site linear optomechanical coupling by $g_0 = g_{\text{om}}x_{\text{zpf}}$ (x_{zpf} is the displacement due to zero point fluctuations)¹⁸. The effective mass associated to the oscillator can be estimated as $m_{\text{eff}} \sim 0.5\text{ pg}$ for a structure of $2\mu\text{m}$ lateral size (see the Supplementary Material V) and from this we obtain $x_{\text{zpf}} \sim 1\text{ fm}$. It follows that $g_0/2\pi \sim 50\text{ MHz}$, quite a huge value when compared with other reported optomechanical systems.¹⁸ By involving the deformation potential interaction associated to the exciton component of polaritons, $g_0/2\pi$ is thus amplified by three orders of magnitude from the $\sim 50\text{kHz}$ calculated for purely optical radiation pressure interaction.³⁹ To enhance cavity optomechanical phenomena materials with electronic resonances are usually avoided due to the related absorption that reduces the optical Q-factor.¹⁸ Counter intuitively, the contrary occurs in our polaromechanical crystals. Indeed, the measured BEC coherence time is $\sim 1 - 2\text{ ns}$, implying $Q \sim 7 \times 10^5$, while the bare cavity photon lifetime is only $\sim 10\text{ ps}$. This means that by involving the exciton-mediated optomechanical interaction g_0 is amplified by three orders of magnitude, while at the same time because the system is in the (polariton) strong coupling regime the Q-factor is *enhanced* by a factor ~ 100 .

DATA AVAILABILITY

The source data that support the findings of this study are available from the corresponding author upon reasonable request. All these data are directly shown in the corresponding figures without further processing.

* Corresponding author, e-mail: afains@cab.cnea.gov.ar

REFERENCES

¹ G. Kurizkia, P. Bertetb, Y. Kubob, K. Molmerc, D. Petrosyand, P. Rablf, and J. Schmiedmayerf, Quantum technologies with hybrid systems, Proc. Nat. Acadm. Science **112**, 3866 (2015).

² J. Kasprzak, M. Richard, S. Kundermann, A. Baas, P. Jeambrun, J. M. J. Keeling, F. M. Marchetti, M. H. Szymańska, R. André, J. L. Staehli, V. Savona, P. B. Littlewood, B. Deveaud, and L. S. Dang, Bose-Einstein Condensation of Exciton Polaritons, Nature (London) **443**, 409 (2006).

³ A. Amo, D. B. D. Sanvitto, F. Laussy, E. del Valle, M. Martin, A. Lemaître, J. Bloch, D. Krizhanovskii, M. Skolnick, C. Tejedor, and L. Viña, Collective Fluid Dynamics

of a Polariton Condensate in a Semiconductor Microcavity, *Nature (London)* **457**, 291 (2009).

⁴ K. G. Lagoudakis, B. Pietka, M. Wouters, R. André, and B. Deveaud-Plödran, Coherent oscillations in an exciton-polariton Josephson junction, *Phys. Rev. Lett.* **105** 120403 (2010).

⁵ M. Abbarchi, A. Amo, V. G. Sala, D. D. Solnyshkov, H. Flayac, L. Ferrier, I. Sagnes, E. Galopin, A. Lemaître, G. Malpuech, and J. Bloch, Macroscopic quantum self-trapping and Josephson oscillations of exciton polaritons, *Nature Physics* **9** 275 (2013).

⁶ I. Carusotto, and C. Ciuti, Quantum fluids of light, *Reviews of Modern Physics* **85**, 299 (2013).

⁷ M. J. Hartmann, F. G. Brandao, and M. B. Plenio, Strongly interacting polaritons in coupled arrays of cavities, *Nature Physics* **2**, 849 (2006).

⁸ K. Winkler, J. Fischer, A. Schade, M. Amthor, Robert Dall, Jonas Gessler, M. Emmerling, E. A. Ostrovskaya, M. Kamp, C. Schneider, and S. Höfling, A polariton condensate in a photonic crystal potential landscape, *New J. Phys.* **17**, 023001 (2015).

⁹ S. Alyatkin, H. Sigurdsson, A. Askopoulos, J. D. Töpfer, and P. G. Lagoudakis, Interaction induced point scatterer lattices and flat band condensation of exciton-polaritons, *arXiv:2007.02807* (2020).

¹⁰ K. P. Kalinin, and N. G. Berloff, Toward Arbitrary Control of Lattice Interactions in Nonequilibrium Condensates, *Advanced Quantum Technologies* **3** 1900065 (2020).

¹¹ N. Y. Kim and Y. Yamamoto, Exciton-Polariton Quantum Simulators, D. Angelakis (eds), *Quantum Simulations with Photons and Polaritons*, Quantum Science and Technology, Springer (2017).

¹² K. P. Kalinin, A. Amo, J. Bloch, and N. G. Berloff, Polaritonic XY-ising machine, *Nanophotonics* **9**, 4127-4138 (2020)

¹³ T. Boulier, MJ Jacquet, A. Maître, G. Lerario, F. Claude, S. Pigeon, Q. Glorieux, A. Amo, J. Bloch, A. Bramati, and E. Giacobino, Microcavity polaritons for quantum simulation, *Advanced Quantum Technologies* **3**, 2000052 (2020).

¹⁴ S. Ghosh, and T. C. Liew, Quantum computing with exciton-polariton condensates, *Quantum Information* **6**, 1 (2020).

¹⁵ D. D. Solnyshkov, G. Malpuech, P. St-Jean, S. Ravets, J. Bloch, and A. Amo, Microcavity polaritons for topological photonics, *Optical Materials Express* **11**, 1119 (2021).

¹⁶ M. Maldovan, and E. L. Thomas, Simultaneous localization of photons and phonons in two-dimensional periodic structures, *Appl. Phys. Lett.* **88**, 251907 (2006).

¹⁷ M. Eichenfield, J. Chan, R. M. Camacho, K. J. Vahala, and O. Painter, Optomechanical crystals, *Nature* **462** 78 (2009).

¹⁸ M. Aspelmeyer, T. J. Kippenberg, and F. Marquardt, Cavity Optomechanics, *Rev. Mod. Phys.* **86**, 1391 (2014).

¹⁹ H. Ren, M. H. Matheny, G. S. MacCabe, J. Luo, H. Pfeifer, M. Mirhosseini, and O. Painter, Two-dimensional optomechanical crystal cavity with high quantum cooperativity, *Nat. Commun.* **11**, 3373 (2020).

²⁰ M. Schmidt, S. Kessler, V. Peano, O. Painter, and F. Marquardt, Optomechanical creation of magnetic fields for photons on a lattice, *Optica* **2**, 635 (2015).

²¹ Z. Shen, Y-L. Zhang, Y. Chen, F-W. Sun, X-B. Zou, G.-C. Guo, C-L. Zou, and C.-H. Dong, Reconfigurable optomechanical circulator and directional amplifier, *Nature Communications* **9**, 1797 (2018).

²² F. Ruesink, J. P. Mathew, M-A. Miri, Andrea Alù, and E. Verhagen, Optical circulation in a multimode optomechanical resonator, *Nature Communications* **9**, 1798 (2018).

²³ C. Brendel, V. Peano, O. J. Painter, and F. Marquardt, Pseudomagnetic fields for sound at the nanoscale, *Proc. Natl Acad. Sci. USA* **114**, E3390 (2017).

²⁴ J. P. Mathew, J. del Pino, and E. Verhagen, Synthetic gauge fields for phonon transport in a nano-optomechanical system, *Nature Nanotechnology* **15**, 198 (2020).

²⁵ P. Forn-Díaz, L. Lamata, E. Rico, J. Kono, and E. Solano, Ultrastrong coupling regimes of light-matter interaction, *Rev. Mod. Phys.* **91**, 025005 (2019).

²⁶ A. Frisk Kockum, A. Miranowicz, A., S. De Liberato, S. Savasta, and F. Nori, Ultrastrong coupling between light and matter, *Nat Rev Phys* **1**, 19 (2019).

²⁷ S. Hughes, A. Settimeri, S. Savasta, and F. Nori, Resonant Raman scattering of single molecules under simultaneous strong cavity coupling and ultrastrong optomechanical coupling in plasmonic resonators: Phonon-dressed polaritons, *Phys. Rev. B* **104**, 045431 (2021).

²⁸ A. Fainstein, N. D. Lanzillotti-Kimura, B. Jusserand, B. Perrin, Strong optical-mechanical coupling in a vertical GaAs/AlAs microcavity for subterahertz phonons and near-infrared light, *Physical Review Letters* **110**, 037403 (2013).

²⁹ J. Restrepo, C. Ciuti, and I. Favero, Single-polariton optomechanics, *Phys. Rev. Lett.* **112**, 013601 (2014).

³⁰ B. Jusserand, A. N. Poddubny, A. V. Poshakinskiy, A. Fainstein, and A. Lemaître, Polariton Resonances for Ultrastrong Coupling Cavity Optomechanics in GaAs-AlAs Multiple Quantum Wells, *Phys. Rev. Lett.* **115**, 267402 (2015).

³¹ A. S. Kuznetsov, D. H. O. Machado, K. Biermann, and P. V. Santos, Electrically Driven Microcavity Exciton-Polariton Optomechanics at 20 GHz, *Physical Review X* **11**, 021020 (2021).

³² F. Lemoult, N. Kaina, M. Fink, and G. Leproux, Wave propagation control at the deep subwavelength scale in metamaterials, *Nature Physics* **9**, 55 (2013).

³³ A. S. Kuznetsov, P. L. J. Helgers, K. Biermann, and P. V. Santos, Quantum Confinement of Exciton-Polaritons in Structured (Al,Ga)As Microcavity, *Phys. Rev. B* **97**, 195309 (2018).

³⁴ C. Thomsen, H. T. Grahn, H. J. Maris, and J. Tauc, Surface generation and detection of phonons by picosecond light pulses, *Phys. Rev. B* **34**, 4129 (1986).

³⁵ O. Matsuda, T. Tachizaki, T. Fukui, J. J. Baumberg, and O. B. Wright, Acoustic phonon generation and detection in GaAs/Al_{0.3}Ga_{0.7} As quantum wells with picosecond laser pulses, *Phys. Rev. B* **71**, 115330 (2005). Coherent generation of acoustic phonons in an optical microcavity, *Phys. Rev. Lett.* **99**, 217405 (2007).

³⁶ N. D. Lanzillotti-Kimura, A. Fainstein, B. Perrin, and B. Jusserand, Theory of Coherent Generation and Detection of THz acoustic phonons using Optical Microcavities, *Phys. Rev. B* **84**, 064307 (2011).

³⁷ E. Wertz, L. Ferrier, D. D. Solnyshkov, R. Johne, D. Sanvitto, A. Lemaître, I. Sagnes, R. Grousson, A. V. Kavokin, P. Senellart, G. Malpuech, and J. Bloch, Spontaneous formation and optical manipulation of extended polariton condensates, *Nature Physics* **6**, 860 (2010).

³⁸ T. K. Paraïso, M. Kalaei, L. Zang, H. Pfeifer, F. Marquardt, and O. Painter, Squared Coupling in a Tunable

Photonic Crystal Optomechanical Cavity, *Phys. Rev. X* **5**, 041024 (2015).

³⁹ Villafaña, V., P. Sesin, P. Soubelet, S. Anguiano, A. E. Bruchhausen, G. Rozas, C. Gomez Carbonell, A. Lemaître, and A. Fainstein, Optoelectronic forces with quantum wells for cavity optomechanics in GaAs/AlAs semiconductor microcavities, *Physical Review B* **97**, 195306 (2018).

⁴⁰ Wouters, Synchronized and desynchronized phases of coupled nonequilibrium exciton-polariton condensates, *Physical Review B* **77**, 121302 (2008).

⁴¹ H. Ohadi, R.L. Gregory, T. Freegarde, Y. G. Rubo, A. V. Kavokin, N. G. Berloff, and P. G. Lagoudakis, Nontrivial phase coupling in polariton multiplets. *Physical Review X* **6**, 031032 (2016).

⁴² H. Ohadi, Y. D. V. I. Redondo, A. J. Ramsay, Z. Hatzopoulos, T. C. H. Liew, P. R. Eastham, P. G. Savvidis, and J. J. Baumberg, Synchronization crossover of polariton condensates in weakly disordered lattices, *Phys. Rev. B* **97**, 195109 (2018).

⁴³ J. D. Töpfer, H. Sigurdsson, S. Alyatkin, and P. G. Lagoudakis, Lotka-Volterra population dynamics in coherent and tunable oscillators of trapped polariton condensates, *Phys. Rev. B* **102**, 195428 (2020).

⁴⁴ A. Pikovsky, M. Rosenblum, and J. Kurths, *Synchronization, A Universal Concept in Nonlinear Sciences* (Cambridge University Press, 2001).

⁴⁵ N. Lörch, S. E. Nigg, A. Nunnenkamp, R. P. Tiwari, and C. Bruder, Quantum synchronization blockade: Energy quantization hinders synchronization of identical oscillators, *Phys. Rev. Lett.* **118**, 243602 (2017).

⁴⁶ M. F. Pascual-Winter, A. Fainstein, B. Jusserand, B. Perrin, and A. Lemaître, Phonon optical generation and detection spectral responses in superlattices, *Rev. B* **85**, 235443 (2012).

⁴⁷ P. Ruello and V. E. Gusev, Physical mechanisms of coherent acoustic phonons generation by ultrafast laser action, *Ultrasonics* **56**, 21 (2015).

⁴⁸ D. L. Chafatinos, A. S. Kuznetsov, S. Anguiano, A. E. Bruchhausen, A. A. Reynoso, K. Biermann, P. V. Santos, and A. Fainstein, Polariton-driven phonon laser, *Nature Communications* **11**, 4552 (2020).

ACKNOWLEDGMENTS

We acknowledge partial financial support from the ANPCyT-FONCyT (Argentina) under grants PICT-2015-1063, PICT-2018-03255, PICT-2016-0791 and PICT 2018-1509, CONICET grant PIP 11220150100506, SeCyT-UNCuyo grant 06/C603, from the German Research Foundation (DFG) under grant 359162958, and the joint Bilateral Cooperation Program between the German Research Foundation (DFG) and the Argentinian Ministry of Science and Technology (MINCyT) and CONICET. AF thanks the Alexander von Humboldt Foundation for the support, and the Paul Drude Institute for the hospitality during which this work was finished.

AUTHOR CONTRIBUTIONS

D.L.C. and A.S.K. have contributed equally. D.L.C, I.P. and A.E.B. contributed to the pump and probe and locking experiments, and A.S.K to the sample characterization and measurement of the polariton dispersions. A.S.K., K.B., and P.V.S. designed and fabricated the structured microcavity sample. P.S., A.A.R., G.U, A.E.B., and A.F. outlined the theoretical aspects. All authors contributed to the discussion and analysis of the results. P.V.S. and A.F. conceived and directed the project. A.F. prepared the manuscript with inputs from all co-authors.

COMPETING INTERESTS

The authors declare no competing interests.

ADDITIONAL INFORMATION

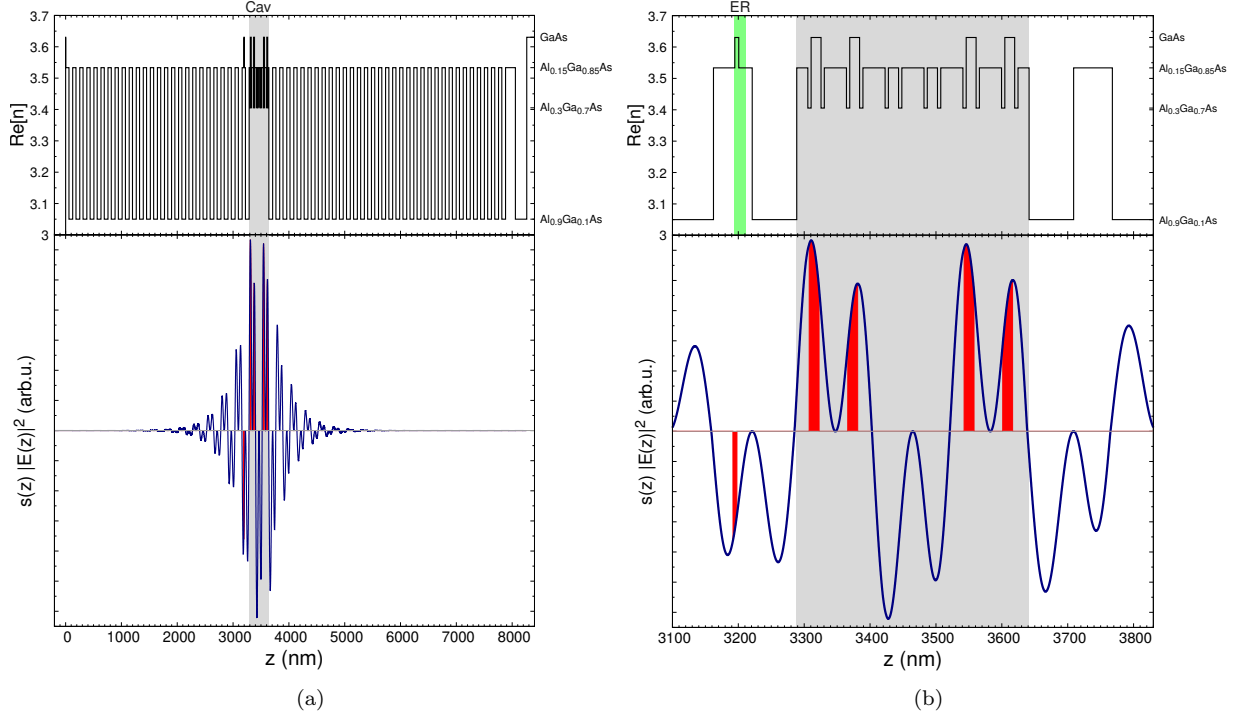
Supplementary information is available for this paper at <https://doi.org/...>

Correspondence and requests for materials should be addressed to A.F.

Supplementary Material for: Metamaterials of Fluids of Light and Sound

This Supplementary Material includes: [Supplementary Note 1](#)) A description of the hybrid microstructured devices that confine polaritons and phonon in traps and arrays of traps, [Supplementary Note 2](#)) the experimental method used to investigate the phonons in the hybrid phonon-polariton traps, [Supplementary Note 3](#)) experimental results, not shown in the main text, and that might be appropriate for an interested readership, [Supplementary Note 4](#)) several theoretical considerations including details of the finite elements simulations, together with the description of the effective potential model used to describe the phonon experimental results in single traps and trap arrays, and [Supplementary Note 5](#) the outline of how the effective mass of the mechanical mode is defined.

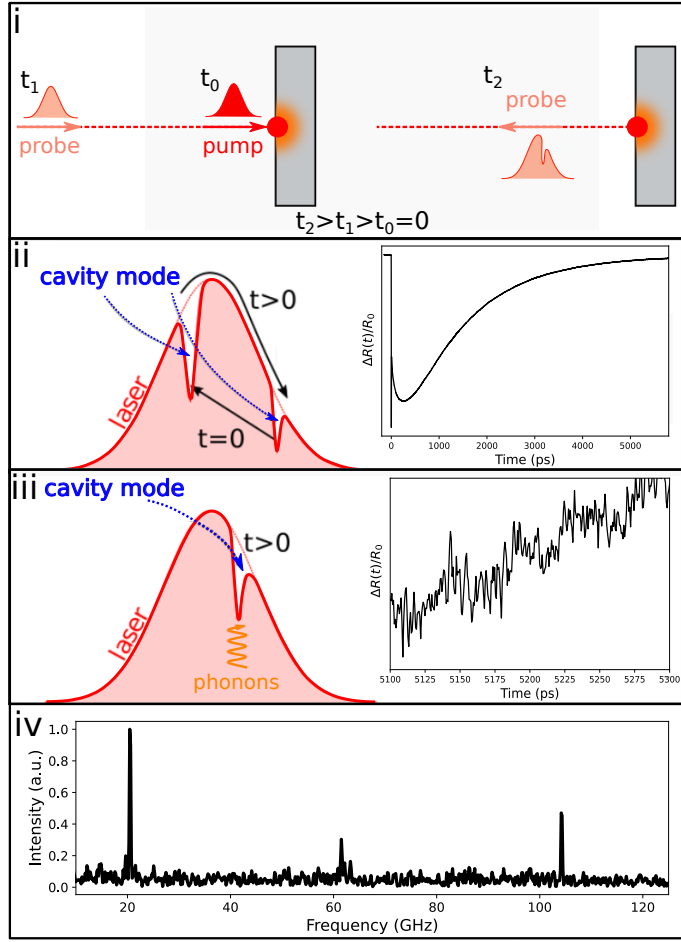
Supplementary Note 1. SAMPLE DETAILS AND DESCRIPTION



Supplementary Figure S1. **Sample's structure and strain-electric field overlap.** (a) The top panel displays the profile of the real part of the index of refraction (n) along the MBE growth direction z . $z=0$ nm corresponds to the air-sample surface, and the substrate begins at $\sim 8.2 \mu\text{m}$. Top and bottom DBRs are separated by the cavity spacer (gray shaded region, Cav) that embeds the four GaAs QWs. The bottom panel shows the overlap between the strain field $s(z)$ and the squared electric field $|E(z)|^2$. (b) corresponds to the detail of the cavity region in (a). The green area (ER) corresponds to the part that is removed during the etching process. The optimized overlap of $s(z) |E(z)|^2$ with the GaAs cavity QWs is indicated in red.

Figure S1(a) (top panel) shows a scheme of the profile of the planar sample. Here the real part of the refractive index corresponding to each layer is plotted as a function of the MBE growth direction (z). Figure S1(b) details the region of the hybrid photon/phonon cavity with the embedded QW's. The region of the cavity is highlighted in gray, and the region (ER) highlighted in green in the top panel of Fig. S1(b) corresponds to the portion of the sample (~ 12 nm) that is removed during the etching process to attain the in-plane patterning required to define the traps [see Fig. 1(a) of the main text].

The microcavities reported in this work were designed to optimize the *electrostrictive polariton-phonon interaction*. To achieve this situation, the quantum wells (QWs) were displaced from the anti-nodes of the cavity electric field [$|E(z)|$], which turn out to be nodes of the strain field [$s(z)$] to the position were the product $s(z) |E(z)|^2$ is maximized. The bottom panels of the respective Figs. S1(a) and S1(b) show this optimized magnitude along the z -direction for the planar sample. As can be noted, in panel (a) the strain-electric field product is peaked at the cavity spacer, and



Supplementary Figure S2. **Picosecond coherent phonon pump-probe method.** A scheme of this technique is presented in panel (i). At t_0 the pump pulse strikes the sample inducing a change of the refractive index, and launching coherent phonons. At a later time t_1 a delayed pulse probes the cavity reflectivity. The change in the refractive index induces a shift of the cavity mode, leading to the so-called electronic-signal (ii). The coherent phonons modulate the cavity mode leading to the vibrational signal (iii). Processing of the signal obtained as a function of the probe delay, and its Fourier transform, lead to the vibrational spectra (iv). Typical cavity confined modes are observed around 20, 60, and 100 GHz.

the overlap is optimal at the QWs position. This region of QWs and strain-electric field's superposition is indicated by the red-shaded area in Fig.S1(b).

The fabrication method and micrometer size lateral patterning of the traps, in the context of cavity polariton, is well described in Refs.[1–3]. It consists of an MBE growth of the bottom DBR and the cavity spacer with the embedded QWs. The processes continues with the patterning and wet-etching of the traps outside the MBE chamber, and is concluded with a subsequent MBE overgrowth of the top DBR. The sample consisted of a top(bottom) DBR formed by 25(33) $\frac{\lambda}{4}/\frac{\lambda}{4}$ periods of $\text{Al}_{0.15}\text{Ga}_{0.85}\text{As}/\text{Al}_{0.90}\text{Ga}_{0.10}\text{As}$ layers, embedding a $\frac{3}{2}\lambda$ cavity with four 15 nm GaAs QWs as schematized in Fig.S1(b) (top panel), grown on a 350 μm thick GaAs(001) substrate. A scheme of the resulting structure is shown in Fig.1(a) of the main text. One point worth mentioning is that the quality of the QWs is not affected by the etching and overgrowth processes.

Supplementary Note 2. TIME-RESOLVED PUMP-PROBE PHONON SPECTROSCOPY

The method used to investigate the dynamical aspects of the 3D phononic states of the individual traps, as well as the double-coupled trap systems (molecules) and 2D trap arrays, is the ultra-fast laser spectroscopy method called picosecond coherent phonon pump and probe technique,^{4,5} particularly adapted for semiconductor optical microcavities,⁶ combined with microscopy to enable the addressing of individual traps.⁷

The concept of this method is illustrated in Fig. S2(i)-(iii). A ps-laser pulse is used to resonantly excite the optical cavity mode. Because of direct (above-gap excitation) or residual (below-gap excitation) carrier generation, a rapid change of index of refraction is induced by the pump, which recovers within a time-scale defined by electron-hole evolution and recombination. Following this change in the refractive index, the cavity mode strongly blue-shifts in a ps scale, to recover its equilibrium in longer ns-scale times. In addition to this electronic response, the pump pulse through the same carrier excitation launches coherent phonons mediated by a deformation-potential induced displacive mechanism.^{8,9} These mechanical oscillations modulate the cavity energy involving mainly two mechanisms, interface displacement and photoelastic interaction,^{8,9} and can thus be detected using a delayed probe that samples the cavity's reflectivity.^{10,11}

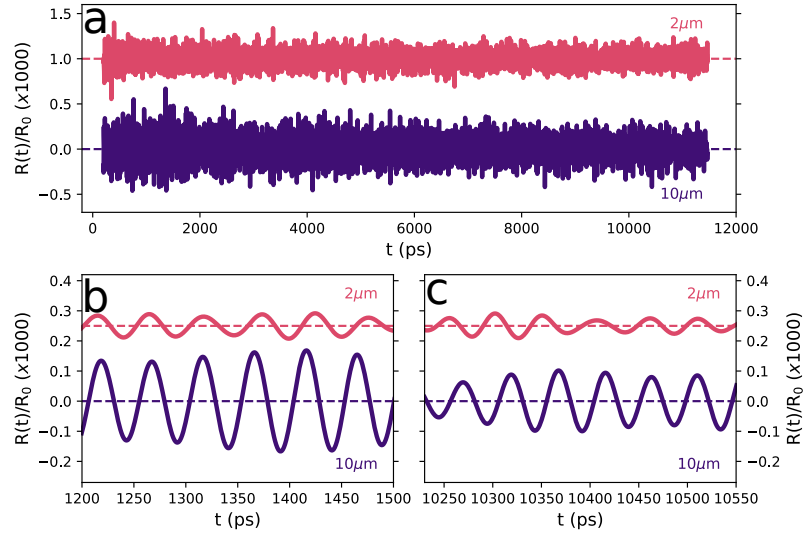
In Fig. S2(ii)(right panel) a typically obtained transient reflectance $\Delta R(t)/R_o$ is shown. The reflectivity of the probe pulse is recorded as a function of the time delay with respect to the arrival of the exciting pump pulse that defines $t=0$ ps. Using a convenient filtering treatment, the slow varying envelope evolution, ascribed to the optical constant's temporal variations due to electronic states and thermal modifications, the faster dynamics defined by the vibrational oscillatory components can be extracted [see right panel in Fig. S2(iii)]. After extraction a spectral analysis is performed by applying a numerical Fourier transformation (nFT) of the measured window.

A typical spectrum is shown in Fig. S2(iv), with the characteristic stronger signal corresponding to the ~ 20 GHz fundamental confined breathing mode of the structures, and weaker contributions at the higher energy overtones at ~ 60 GHz and ~ 100 GHz. These acoustic cavity modes have been previously studied in planar microcavities,⁶ and also in individual micrometer-size pillars obtained by deep etching planar structures.^{12,13} This previous knowledge is exploited here to experimentally identify the phonon confinement in *individual* polariton traps generated by weak distant modulation of the spacer thickness, and is extended to study more complex structures with different dimensionality (molecules, and 2D arrays).

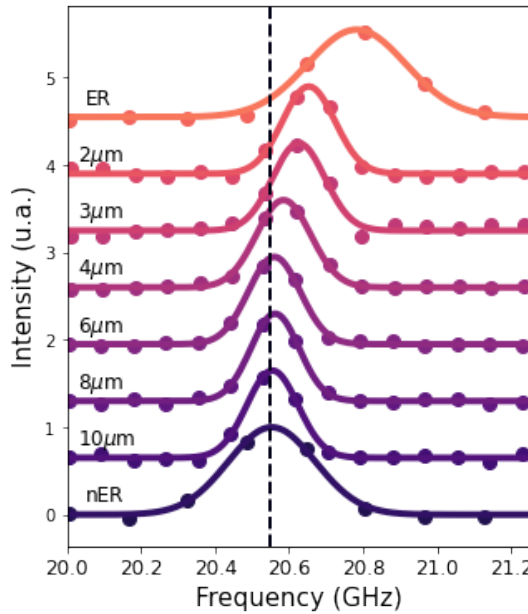
Supplementary Note 3. PHONON CONFINEMENT IN TRAPS: EXPERIMENTAL RESULTS

Examples of measurements using this technique on a single micrometer size polariton trap are depicted in Fig. S3. In panel (a), the transient curves corresponding to the vibrational contributions (the electronic part was removed as explained above), extracted for an isolated $2 \times 2 \mu\text{m}^2$ trap (pink curve), and for an isolated $10 \times 10 \mu\text{m}^2$ trap (violet curve) are shown. Both transients show clear oscillations, which result from the superposition of the spectral components [see Fig. S2(iv)] of ~ 20 , ~ 60 , ~ 100 GHz (periods respectively of ~ 50 , ~ 17 , ~ 10 ps). For the extended temporal scale chosen in Fig. S3(a) the individual oscillations, which are coherent with respect the impulsive excitation of the pump pulse, can not be distinguished. However, it is clearly noticeable that the signal remains basically undamped up to the observed ~ 11 ns (the maximum scan time is limited by the ~ 80 MHz repetition rate of the pulsed laser). It actually well exceeds this wide acquired time frame. To better see this prevalence, in Fig. S3(b) and (c) we show the transient oscillations of the fundamental mode of the traps, filtered using a band-pass ± 3 GHz centered around the fundamental modes (at ~ 20.68 GHz and ~ 20.55 GHz, respectively). Figure S3(b) corresponds to a time window at early delay times, and Fig. S3(c) at almost the end of the measured window. The observation of the vibrational modes of these micrometer size polariton traps, which exhibit lifetimes that well exceed 12 ns, is in contrast to what has been previously observed in optomechanical semiconductor micropillar resonators^{12,14,15}.

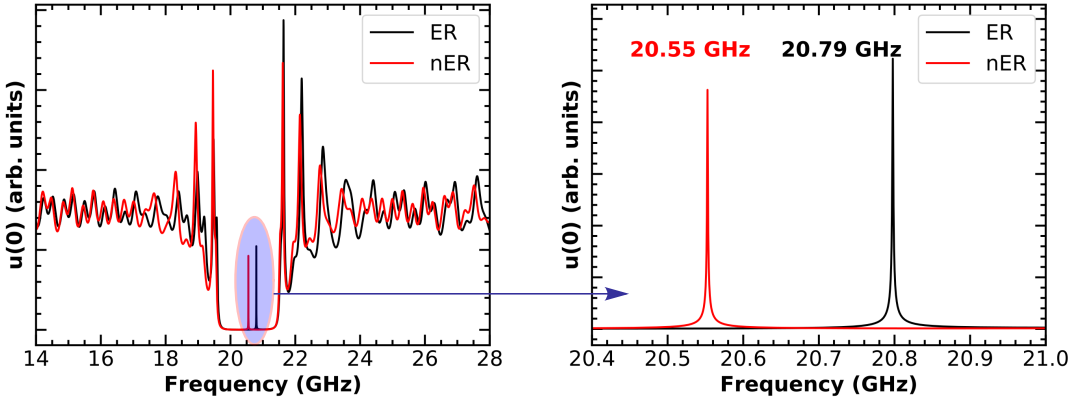
Several single square polariton traps of varying lateral sizes have been analyzed using picosecond coherent time-resolved pump-probe phonon spectroscopy in combination with microscopy. In Fig. S4 we show a detail of the spectral region of the fundamental 3D confined phononic mode around 20 GHz [see Fig. S2(iv)], when varying the trap size as indicated. As a reference, the results for the planar samples on the non-edged (nER) and edged (ER) regions are included. Due to the measured temporal window (same for all traps, see Figs. S3), the spectra are resolution limited. However, the blue-shift for decreasing trap size is clearly observed. The determination of the peaks' position, reported in Fig. 2(c) of the main text, was performed by fitting the data using Gaussian distribution functions. The dotted vertical line indicates the frequency of the non-etched planar sample. The spectra for nER and ER have been measured using a shorter temporal window, with the consequent increase of the Fourier-limited peak's width.



Supplementary Figure S3. **Extracted phonon oscillations for two different isolated traps.** (a) The bottom curve of this panel corresponds to the transient measured on a $10 \times 10 \mu\text{m}^2$ trap, whereas the upper curve correspond to the equivalent results on a $2 \times 2 \mu\text{m}^2$ trap. (b) and (c) correspond to the upper transients in (a) with a band-pass filter centered at 20.55 GHz and 20.68 GHz, respectively. (b) corresponds to a detail for short delay times, whereas (c) displays the situation near the end of the temporal measured window.



Supplementary Figure S4. **Variation with the traps' size of the confined fundamental phonon mode.** Spectra showing the size dependence of the acoustic confined ground state in square traps. Symbols are the experimental results obtained from a numerical Fourier transformation (nFT) of the extracted picosecond coherent time-resolved pump-probe measurements. The continuous curves are the corresponding Gaussian fits. The clear shift is evidenced, due to phonon confinement in the traps, with respect to the planar (non-structured) situation (nER) marked by the vertical dotted line.



Supplementary Figure S5. **Phonon confinement in planar cavities.** The panel on the left shows the calculated surface displacement (equivalent to the transmission) for white sound propagating from the substrate for both the non-etched (nER) and etched (ER) planar regions. The calculations were performed using a transfer matrix method. The phonon cavity mode for each structure can be seen within the phonon DBR stop-bands (detailed with a zoom, right panel). The frequency difference (~ 0.24 GHz) between both modes is a measure of the modulation amplitude for the effective phonon potentials affecting the in-plane propagation of these cavity-confined phonons when the lateral patterning defines the hybrid micrometer-size phonon-polariton traps.

Supplementary Note 4. THEORETICAL CONSIDERATIONS OF PHONON CONFINEMENT IN TRAPS AND ARRAYS OF TRAPS

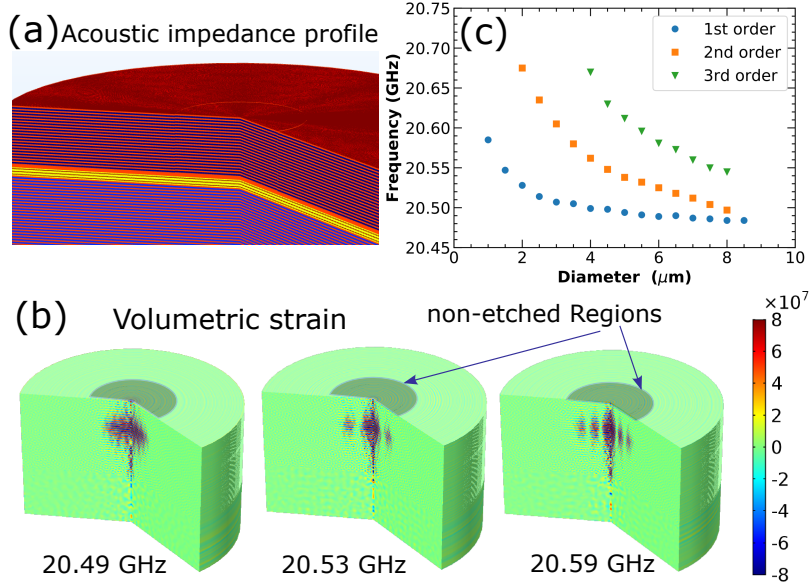
A. Phonon confinement in planar structures

The vertical confinement (along the z direction) is illustrated in Fig. S5, where the calculated acoustic transmission is displayed for the cases of the planar non-etched (nER, red curve) and etched (ER, black curve) regions. The acoustic transmission is evaluated as the frequency resolved surface displacement for “white” sound incident from the substrate. The typical DBR phonon stop-band¹⁶ can be identified between approximately 19.8 and 21.3 GHz.

The simultaneous photon-phonon field’s co-localization of this hybrid device (see main text),⁶ is evidenced for the nER by the cavity mode appearing at the acoustic stop-band’s center (~ 20.55 GHz). The acoustic cavity mode for the ER is blue-shifted out from the stop-band’s center approximately by 0.24 GHz. Extending the same concept used for photonic traps to the acoustic phonons, one concludes that the lateral patterning described above should lead to an additional phononic lateral trapping potential, with modulations of ~ 0.24 GHz between nER and ER regions. This potential should determine the in-plane propagation of the vertically confined acoustic phonons in a way that should be fully equivalent to the described confinement of photons.³

B. 3D Phonon confinement: Finite elements calculation

To test and demonstrate the concept of lateral in-plane effective confinement in these kind of traps, we calculated the mechanical eigenmodes using a commercial finite elements analysis software (COMSOL Multiphysics¹⁷) for the simplest geometry: a circular trap of cylindrical symmetry. GaAs and AlAs are considered as mechanically isotropic materials, and no mechanical absorption processes are considered. The used geometry is presented in Fig. S6(a). The material layering shown in this panel corresponds to the nominal values as defined by the MBE growth. The trap is modeled as a central circular region with larger spacer thickness as prescribed by the performed microfabrication process, and consistent with the measured polariton confinement (Fig. Fig1(a) of the main text). The full calculated structure is a cylindrical pillar limited by vacuum. In contrast with the optical response of the structure, phonons are subject to total reflection at the semiconductor/vacuum interfaces. To avoid any artificial effect induced by the pillar geometry, for the calculations we chose a total diameter large enough so that the free boundary condition of the sample-vacuum interfaces do not affect the solutions of modes localized at the smaller trap centered at the pillar. Also, in contrast with the light wave solutions, different mechanical directions of vibration are coupled through the Poisson’s ratio (the ratio of transverse to axial elastic strain). In our case, a mode fulfills two simultaneous resonance conditions: the vertical confinement, determined by the DBRs and the spacer thickness, and the radial confinement



Supplementary Figure S6. **Phonon confinement in microcavity 3D traps.** Finite-elements 3D modeling of the spatial distribution and lateral size energy dependence, respectively, of the acoustic modes of single circular traps. (a) A detail of the modeled circular traps is presented, where the layered structure consists of: The top and bottom DBRs (indicated with red and violet layers, respectively), the spacer (yellow), and the patterned region (orange). The calculation is performed for a large cylindrical pillar of $20\mu\text{m}$ in diameter. At the center of this cylinder, the trap with the larger spacer thickness is patterned. The circular step forming the disk, is visible at the upper air-sample surface of this sketch (see text for details). In (b) the simulated volumetric strain ($\Delta v/V$) for first three confined mechanical modes is shown for a circular trap of a $5.5\mu\text{m}$ diameter trap. (c) Results for the calculated frequency of the first three orders of mode confinement for corresponding varying trap diameter.

determined by the effective potential induced by the local variation of the spacer thickness. Fulfilling both conditions results in a coupling between vertical and radial strains described by Poisson's ratio. Traps of diameter from $1\text{-}8\mu\text{m}$ were modeled, choosing $20\mu\text{m}$ for the external pillar diameter, and all the structure mounted on a $5\mu\text{m}$ thick GaAs substrate.

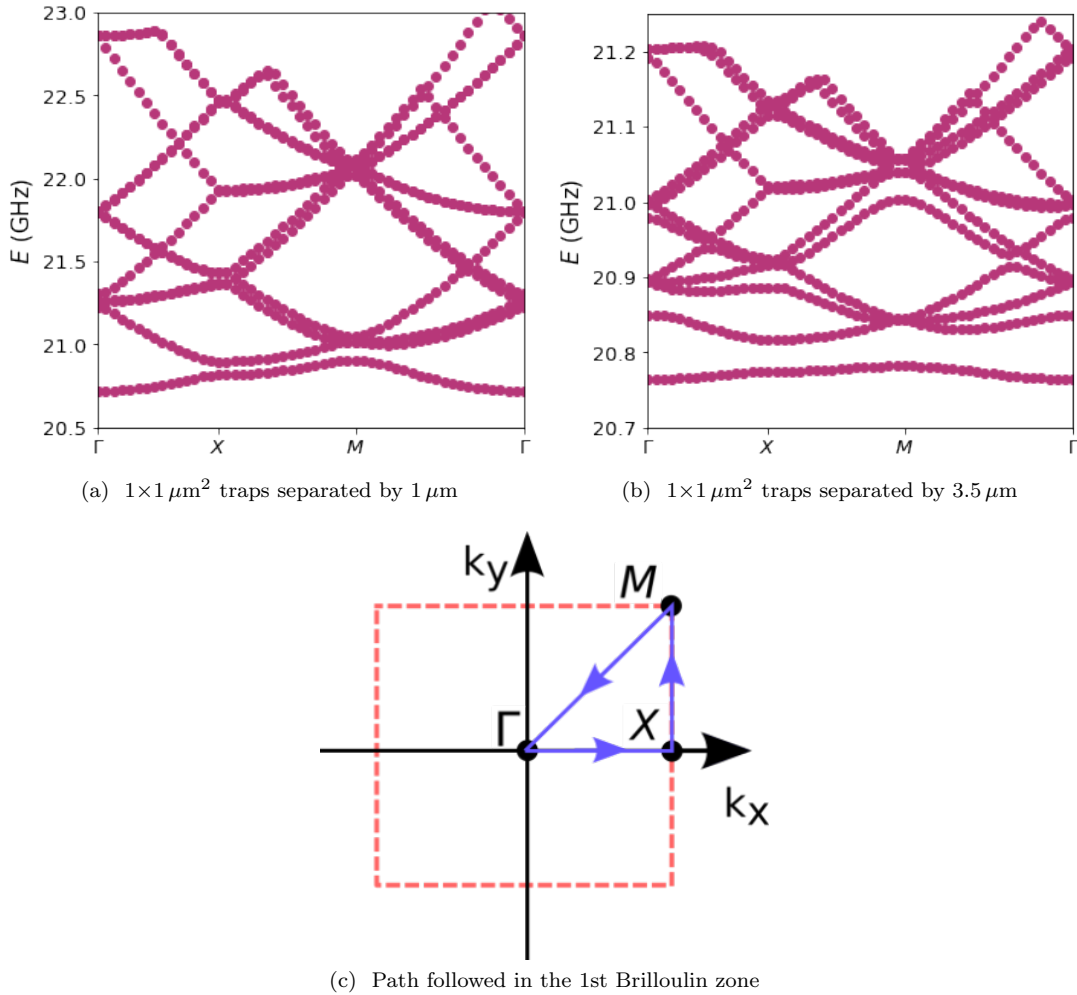
As the material parameters, such as density, Young's modulus, and the Poisson ratio, well established and published values were used for the $\text{Al}_x\text{Ga}_{1-x}\text{As}$ layered system.¹⁸ The volumetric strain ($\Delta v/V$) for the mechanical fundamental eigenmode and the first two excited eigenmodes, for a $5.5\mu\text{m}$ diameter trap are shown in Fig. S6(b). These modes correspond to laterally well localized symmetric vibrations with different number of radial nodes. The trap-size dependence of the frequency of these modes is presented in Fig. S6(c), showing the expected $1/D$ increase with decreasing diameter D . For the ground state this confinement induced blue-shift amounts to somewhat less than 100 MHz for $D \sim 1\mu\text{m}$. Quite clearly the mechanical modes become strongly localized within the trap by the effective potential and, interestingly, due to the Poisson-ratio the breathing-like character of the modes implies that an expansion(compression) along z is accompanied by an in-plane compression(expansion).

C. Effective potential model and phonon trap lattices

As addressed and demonstrated in the previous subsection [Supplementary Note 4 A](#) and [Supplementary Note 4 B](#), the traps perform as resonators that confine phonons in all three dimensions. In addition, the finite height of the phonon effective potential barriers allows for the design of lattices, with the concomitant emergence of acoustic 2D phonon bands, in a similar way as what happens to polatitons and is illustrated in Fig. 1(d) of the main text.

For modeling how the cavity phonon mode's energy is affected by the different trap and array configurations (isolated traps, double-traps, and 2D arrays) we start from the non-etched effective quadratic dispersion relation arising when k_z is quantized, i.e.

$$E(k_x, k_y) = E_{\text{cav,ne}} + \frac{\hbar^2(k_x^2 + k_y^2)}{2m_{\text{eff}}}.$$



Supplementary Figure S7. Phonons in polariton-phonon hybrid lattices. The in-plane dispersion of the acoustic modes of a square lattice of $1 \times 1 \mu\text{m}^2$ square traps, separated by 1 and $3.5 \mu\text{m}$, respectively in (a) and (b). (c) depict the path followed in the first Brillouin zone and shown in (a) and (b).

Notice that for a material with homogeneous speed of sound v_s the effective mass $m_{\text{eff}} = E_{\text{cav,ne}}/v_s^2$. Such a effective mass description of the unconfined non-etched zone is incorporated in a 2D Schrödinger equation,

$$\left[-\frac{\hbar^2}{2m_{\text{eff}}} \nabla^2 + E_{\text{cav,ne}} + V_e(x, y) \right] \Psi(x, y) = E \Psi(x, y) ,$$

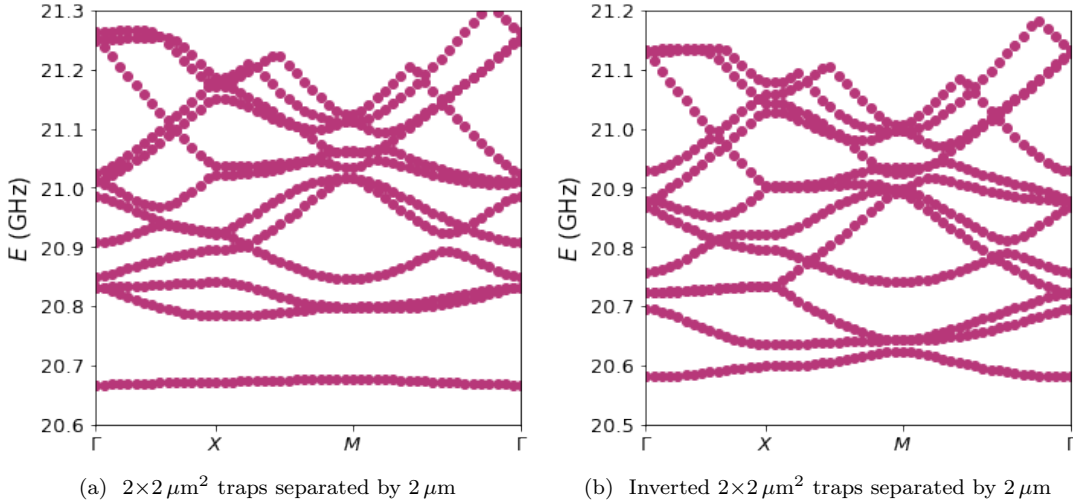
that adds, via the potential $V_e(x, y)$, the effect of the trapping induced by the etching. Taking into account that the energy of the phonon mode in a large etched region is $E_{\text{cav,e}}$ we can assume that the full height of the potential in an etched zone is $V_{\text{max}} = (E_{\text{cav,e}} - E_{\text{cav,ne}})$. Consequently, each square trap with a given index i , centered at (x_i, y_i) contributes to $V_e(x, y)$ the potential

$$V_i(x, y) = V_{\text{max}} [1 - v_i(x - x_i)v_i(y - y_i)]$$

where, following Ref.[3], the profile of the trap “ i ” along each direction is given by

$$v_i(\alpha) = \frac{1}{2} \left[\text{erfc} \left(\frac{\alpha - \frac{w_i}{2}}{0.55 \delta_i} \right) - \text{erfc} \left(\frac{\alpha + \frac{w_i}{2}}{0.55 \delta_i} \right) \right] ,$$

where w_i is the trap width, δ_i is the 10% to 90% transition length, and $\text{erfc}(\dots)$ stands for the *complementary error function*. Using finite differences we solve the eigenvalue problem by discretising a large 2D zone containing the traps. For the case of molecules and arrays, all traps have $w_i = w$ and are separated by the distance Δ . The simulated zone restricts to the supercell, where the super-lattice spacing is $a = w + \Delta$. After the numerical calculation, we obtain the eigen-energies for each value of \mathbf{k} (1D or 2D) by the customary approach of imposing periodic conditions that fulfill



Supplementary Figure S8. **Phonons in polariton-phonon hybrid lattices: comparison with inverted potential lattices.** (a) In-plane dispersion of the acoustic modes of a square lattice of $2 \times 2 \mu\text{m}^2$ squared traps, separated by $2 \mu\text{m}$. (b) Complementary lattice to (a) where the etched and non-etched regions are permuted.

the Bloch's theorem. For the width of the transition regions between the nER to ER, we take $0.35 \mu\text{m}$, consistent with both the modeling of the polariton properties and scanning tunneling microscopy (STM) studies in similar structures³.

Results of calculations using the above described effective model, are shown in Figs. S7 and S8. In Fig. S7(a), the acoustic phonon 2D band dispersion relation within the first Brillouin zone is shown for the case of a square array of $1 \times 1 \mu\text{m}^2$ traps separated by $1 \mu\text{m}$. The acoustic dispersion follows the usual path in k -space, i.e. $\Gamma \rightarrow X \rightarrow M \rightarrow \Gamma$, as indicated in panel (c) of the figure. Figure S7(b) corresponds to the acoustic phonon 2D band dispersion relation for the same square array of $1 \times 1 \mu\text{m}^2$ traps, but the distance between traps is enlarged to $3.5 \mu\text{m}$.

Referring back to the dispersion relation shown in Fig. 1d of the main text, we note that as for the polariton case presented in Fig. 1c, the isolated $1 \times 1 \mu\text{m}^2$ square traps only sustain one single confined state, all other states belonging to the continuum. Consequently, for the two presented arrays a single (lower energy) tight-binding-like band is formed, corresponding to a *flat-band situation* for the thick $3.5 \mu\text{m}$ barriers (massive phonons), and a broad-band (lighter phonons) for the thinner $1 \mu\text{m}$ barriers. All other bands are similar in the two cases, resembling free-electron-like physics. The consequence is that a full 3D phonon gap around $\sim 20.8 \text{ GHz}$ only exists for the thicker studied barrier. The different bands result from the coupling of the discrete energy levels that are confined in 0D in each trap. For example, the lower energy band in Fig. 1d of the main text arises mainly from the fully confined s-like ground state of the phonon trap, and thus displays a tight-binding-like parabolic dependence around the Γ point equivalent to the polariton one in panel c of that same figure. The s-like character refers here to the in-plane spatial distribution of the mode within the trap. For this modelled structure with small traps, the higher states are not confined and thus resemble those of almost free-electrons in a lattice. As a result the second band in Fig. 1d has a preponderant p-like character, but it is also mixed with trap levels of higher order. Summing-up this section, it is thus clear that the proposed technology can be used for phonon engineering in 2D based on acoustic nanocavities, as has been previously proposed theoretically to obtain phonon molecules, band structures, and acoustic Bloch oscillations using simpler 1D layered media.^{19,20}

Additionally, in Fig. S8 two further examples of 2D dispersion for two trap arrays are shown. Panel (a) corresponds to a square array of $2 \times 2 \mu\text{m}^2$ traps separated by $2 \mu\text{m}$, and (b) for the inverted complementary structure, i.e. the regions that were etched and non-etched are inverted. The path followed to draw the 2D dispersions is the same as the one shown previously in Fig. S7(c).

Supplementary Note 5. CALCULATION OF THE EFFECTIVE MASS OF THE INVOLVED ACOUSTIC MODE

In order to obtain the effective mass (m_{eff}), a parameter that is usually used to describe the optomechanical coupling between the fundamental confined photonic (polaritonic) mode with the fundamental confined acoustic mode, we consider the involved potential energy. The general phonon displacement $\vec{U}(\vec{r})$ of the acoustic mode can be parameterized as $\vec{U}(\vec{r}) = u_0 \vec{u}(\vec{r})$, where $\vec{u}(\vec{r})$ corresponds to the normalized displacement mode. The normalization of this mechanical mode is considered in such a way that at position \vec{r}_0 , $|\vec{U}(\vec{r}_0)|^2 \equiv 1$. \vec{r}_0 is defined as the reduction point and is chosen as the position where the modes displacement is maximal.²² For our system, the reduction point is situated at the interfaces of the phonon cavity spacer (see Sec. [Supplementary Note 1](#)). The potential energy of the parameterized mechanical oscillator must be equal to the actual potential energy of the confined phonon breathing mode:

$$\frac{1}{2} \Omega_M^2 \int d^3 \vec{r} \rho(\vec{r}) |\vec{U}(\vec{r})|^2 = \frac{1}{2} \Omega_M^2 m_{\text{eff}} u_0^2 .$$

Consequently, the effective mass is obtained as

$$m_{\text{eff}} = \frac{\int d^3 \vec{r} \rho(\vec{r}) |\vec{U}(\vec{r})|^2}{u_0^2} \equiv \int d^3 \vec{r} \rho(\vec{r}) |\vec{u}(\vec{r})|^2 ,$$

where $\rho(\vec{r})$ is the density distribution field of the structure.

The parameterized effective equation of motion for the cavity confined breathing mode, corresponding to a damped driven oscillator, will be given by²³

$$m_{\text{eff}} \frac{d^2 u}{dt^2} + m_{\text{eff}} \Gamma_M \frac{du}{dt} + m_{\text{eff}} \Omega_M^2 u = F .$$

Here m_{eff} is the effective mode's mass, and Γ_M represents the mechanical damping. The driving force F of the effective mechanical system involves the sum of different contributions, such as radiation pressure (F_{RP}) and electrostrictive (F_{ES}).

* Corresponding author, e-mail: afains@cab.cnea.gov.ar

SUPPLEMENTARY REFERENCES

- ¹ O. El Daif, A. Baas, T. Guillet, J.-P. Brantut, R. I. Kaitouni, J. L. Staehli, F. Morier-Genoud, and B. Deveaud, Polariton quantum boxes in semiconductor microcavities, *Appl. Phys. Lett.* **88**, 061105 (2006).
- ² K. Winkler, J. Fischer, A. Schade, M. Amthor, Robert Dall, Jonas Gessler, M. Emmerling, E. A. Ostrovskaya, M. Kamp, C. Schneider, and S. Höfling, A polariton condensate in a photonic crystal potential landscape, *New J. Phys.* **17**, 023001 (2015).
- ³ A. S. Kuznetsov, P. L. J. Helgers, K. Biermann, and P. V. Santos, Quantum Confinement of Exciton-Polaritons in Structured (Al,Ga)As Microcavity, *Phys. Rev. B* **97**, 195309 (2018).
- ⁴ C. Thomsen, H. T. Grahn, H. J. Maris, and J. Tauc, Surface generation and detection of phonons by picosecond light pulses, *Phys. Rev. B* **34**, 4129 (1986).
- ⁵ O. Matsuda, T. Tachizaki, T. Fukui, J. J. Baumberg, and O. B. Wright, Acoustic phonon generation and detection in GaAs/Al_{0.3}Ga_{0.7} As quantum wells with picosecond laser pulses, *Phys. Rev. B* **71**, 115330 (2005).
- ⁶ A. Fainstein, N. D. Lanzillotti-Kimura, B. Jusserand, B. Perrin, Strong optical-mechanical coupling in a vertical GaAs/AlAs microcavity for subterahertz phonons and near-infrared light, *Physical Review Letters* **110**, 037403 (2013).
- ⁷ D. L. Chafatinos, A. S. Kuznetsov, S. Anguiano, A. E. Bruchhausen, A. A. Reynoso, K. Biermann, P. V. Santos, and A. Fainstein, Polariton-driven phonon laser, *Nature Communications* **11**, 4552 (2020).
- ⁸ M. F. Pascual-Winter, A. Fainstein, B. Jusserand, B. Perrin, and A. Lemaître, Phonon optical generation and detection spectral responses in superlattices, *Rev. B* **85**, 235443 (2012).
- ⁹ P. Ruello and V. E. Gusev, Physical mechanisms of coherent acoustic phonons generation by ultrafast laser action, *Ultrasonics* **56**, 21 (2015).
- ¹⁰ N. D. Lanzillotti-Kimura, A. Fainstein, A. Huynh, B. Perrin, B. Jusserand, A. Miard, and A. Lemaître, Coherent generation of acoustic phonons in an optical microcavity, *Phys. Rev. Lett.* **99**, 217405 (2007)

¹¹ N. D. Lanzillotti-Kimura, A. Fainstein, B. Perrin, and B. Jusserand, Theory of Coherent Generation and Detection of THz acoustic phonons using Optical Microcavities, *Phys. Rev. B* **84**, 064307 (2011).

¹² S. Anguiano, A. E. Bruchhausen, B. Jusserand, I. Favero, F. R. Lamberti, L. Lanco, I. Sagnes, A. Lemaître, N. D. Lanzillotti-Kimura, P. Senellart, and A. Fainstein, Micropillar Resonators for Optomechanics in the Extremely High 19-95 GHz Frequency Range, *Phys. Rev. Lett.* **118**, 263901 (2017).

¹³ F. R. Lamberti, Q. Yao, L. Lanco, D. T. Nguyen, M. Esmann, A. Fainstein, P. Sasin, S. Anguiano, V. Villafañe, A. Bruchhausen, P. Senellart, I. Favero, and N. D. Lanzillotti-Kimura, Optomechanical properties of GaAs/AlAs micropillar resonators operating in the 18 GHz range, *Opt. Express* **25**, 24437 (2017).

¹⁴ S. Anguiano, P. Sasin, A. E. Bruchhausen, F. R. Lamberti, I. Favero, M. Esmann, I. Sagnes, A. Lemaître, N. D. Lanzillotti-Kimura, P. Senellart, and A. Fainstein, Scaling rules in optomechanical semiconductor micropillars, *Phys. Rev. A* **98**, 063810 (2018).

¹⁵ S. Anguiano, A. E. Bruchhausen, I. Favero, I. Sagnes, A. Lemaître, N. D. Lanzillotti-Kimura, and A. Fainstein, Optical cavity mode dynamics and coherent phonon generation in high-Q micropillar resonators, *Phys. Rev. A* **98**, 013816 (2018).

¹⁶ M. Trigo, A. Bruchhausen, A. Fainstein, B. Jusserand, and V. Thierry-Mieg, Confinement of Acoustical Vibrations in a Semiconductor Planar Phonon Cavity, *Phys. Rev. Lett.* **89**, 227402 (2002).

¹⁷ See www.comsol.com for details on this commercial general-purpose simulation software for modeling.

¹⁸ S. Adachi, GaAs, AlAs, and $Al_xGa_{1-x}As$: Material parameters for use in research and device applications, *J. Appl. Phys.* **58**, R1 (1985).

¹⁹ A. E. Bruchhausen, N. D. Lanzillotti-Kimura, B. Jusserand, A. Soukiassian, L. Xie, X. Q. Pan, T. Dekorsy, D. G. Schlom, and A. Fainstein. Acoustic confinement phenomena in oxide multifunctional nanophononic devices. *Phys. Rev. Materials* **2**, 106002 (2018).

²⁰ N. D. Lanzillotti-Kimura, A. Fainstein, C. A. Balseiro, and B. Jusserand, Phonon engineering with acoustic nanocavities: Theoretical considerations on phonon molecules, band structures, and acoustic Bloch oscillations, *Phys. Rev. B* **75**, 024301 (2007).

²¹ A. S. Kuznetsov, D. H. O. Machado, K. Biermann, and P. V. Santos, Electrically Driven Microcavity Exciton-Polariton Optomechanics at 20 GHz, *Physical Review X* **11**, 021020 (2021).

²² C. Baker, W. Hease, D.-T. Nguyen, A. Andronico, S. Ducci, G. Leo, and I. Favero, Photoelastic coupling in gallium arsenide optomechanical disk resonators, *Opt. Express* **22**, 14072 (2014).

²³ C. Metzger, I. Favero, A. Ortlieb, and K. Karrai, Optical self cooling of a deformable Fabry-Perot cavity in the classical limit, *Phys. Rev. B* **78**, 035309 (2008).